HHS Public Access

Author manuscript

Nanoscale. Author manuscript; available in PMC 2021 March 15.

Published in final edited form as:

Nanoscale. 2020 June 04; 12(21): 11510–11517. doi:10.1039/d0nr00075b.

An NIR-II/MR dual modal nanoprobe for liver cancer imaging

Ying Ren[†,a,b], **Shuqing He**[†,b,c], **Lakshmi Huttad**[d], **Mei-Sze Chua**[d], **Samuel K. So**[d], **Qiyong Guo**[a], **Zhen Cheng**[b]

[a]Department of Radiology, Shengjing Hospital of China Medical University, Shenyang, 110004, P. R. China.

[b]Molecular Imaging Program at Stanford (MIPS), Bio-X Program, and Department of Radiology, Canary Center at Stanford for Cancer Early Detection, Stanford University, Stanford, California 94305-5344, USA.

[c]Academy for Advanced Interdisciplinary Studies and Department of Biomedical Engineering, Southern University of Science and Technology (SUSTech), Shenzhen 518055, China

[d]Asian Liver Center, Department of Surgery, Stanford University School of Medicine, Stanford University, Stanford, CA 94305, USA

Abstract

Hepatocellular carcinoma (HCC) is a malignancy of the liver worldwide and surgical resection remains the most effective treatment. However, it is still a great challenge to locate small lesions and define the border of diffused HCC even with the help of preoperative imaging examination. Here, we reported a rare-earth-doped nanoparticle $NaGdF_4$:Nd 5%@$NaGdF_4$@Lips (named Gd-REs@Lips), which simultaneously performed powerful functions in both magnetic resonance imaging (MRI) and second near-infrared fluorescence window imaging (NIR-II, 1000–1700 nm). Imaging studies on orthotopic models with xenografts established from HCC patients indicated that Gd-REs@Lips efficiently worked as a T_2-weighted imaging contrast agent to increase the signal intensity difference between liver cancer tissues and surrounding normal liver tissues on MRI, and it can also serve as a negative NIR-II imaging contrast enabling the precise detection of liver cancer. More importantly, benefiting from the high sensitivity of NIR-II imaging, Gd-REs@Lips allowed the visualization of tiny metastasis lesions (2 mm) on the liver surface. It is expected that the dual NIR-II/MRI modal nanoprobe developed holds high potential to fill the gap between the preoperative imaging detection of cancer lesions and intra-operative guidance, and it further brings new opportunities to address HCC-related medical challenges.

1. Introduction

Hepatocellular carcinoma (HCC) is the sixth most common malignancy worldwide, with >800 000 new cases diagnosed in 2018, and it is the fourth leading cause of cancer-related

guoqy@vip.sina.com, zcheng@stanford.edu.

[†]These authors contributed equally to this work.

Conflicts of interest

There are no conflicts to declare.

mortality worldwide.[1–4] For patients with early stage HCC, surgical resection is still the primary method of intervention, with improved survival benefits and low complications.[5] Magnetic resonance imaging (MRI) and computed tomography (CT) are the most common imaging modalities for HCC diagnosis and pre-operative evaluation. Despite the wide use of MRI and CT technologies for detecting and delineating liver tumors before an operation, up to now, surgeons still need to rely on naked-eye observations and palpations to differentiate tumors from healthy liver tissues during operations.[6,7] This is mainly because of the lack of real-time imaging techniques for intra-operative guidance, and the current techniques used are often not sufficiently sensitive for small tumor nodules that may become aggressive after surgery.

Multiple imaging modalities offer extensive opportunities to overcome the limitations of each individual method and fill the gap between pre-operative imaging and intra-operative reality. In recent years, the development of hybrid nanoparticles for multimodal imaging for the pre-operative detection of HCC tumors *via* MRI, followed by intra-operative guidance of HCC excision *via* optical imaging has attracted intense interest.[8–10] For example, Lee *et al.* have developed a targeted Nd^{3+}-doped upconversion nanoparticle (UCNP) integrating MRI and real-time near infrared (NIR) optical imaging within a single platform.[8] Liu *et al.* reported a nanoprobe obtained by embedding a dumbbell-like Au-Fe_3O_4 core in a dense PEG shell whose outer part is modified with Cy5, folic acid (FA), and a Gd complex. Such a nanoprobe can accumulate in the tumor after intravenous injection into mice, which can be detected using both NIR fluorescence and T_1-/T_2-MR imaging.[10] However, most previous research on the preparation of optical imaging-based multimodality probes is limited to the use of NIR-I fluorescent materials (in the window of 700–900 nm). Recently, NIR-II (1000–1700 nm) fluorescence imaging has emerged as a highly attractive optical window for biological imaging because of its numerous merits, including high spatial resolution, deep penetration depth, and low optical absorption and scattering from biological substrates with minimal tissue autofluorescence.[11–13] Among the various NIR-II fluorophores, rare-earth-doped nanoparticles (RENPs) composed of lanthanide ions embedded within an inorganic crystalline host matrix (*e.g.* $NaYF_4$, GdO_2S_2 and CaF_2) emitting NIR-II light have attracted considerable attention because of their large Stokes shifts, narrow and multi-peak emission profiles, long lifetime, and excellent photostability. Particularly, the lack of excitation–emission band overlap and elimination of tissue autofluorescence produce significantly improved signal-to-noise ratios.[12]

Herein, a novel dual imaging modal probe, $NaGdF_4$:Nd 5% @$NaGdF_4$ (Gd-REs) coated with liposomes (named Gd-REs@Lips), was synthesized and used for *in vivo* imaging in both NIR-II and T_2-weighted MRI in an orthotopic patient-derived xenograft mouse model of HCC. This novel probe not only enhanced the ratio of liver tumor to normal tissue signal, but also enabled the precise detection of HCC using NIR-II imaging.

2. Experimental section

2.1 Materials and reagents

Gadolinium(III) acetate hydrate (99%), neodymium(III) acetate hydrate (99.9%), ammonium fluoride (≥99.99%), sodium hydroxide, 1-octadecene (technical grade, 90%),

oleic acid (technical grade, 90%) and cholesterol (Chol) were purchased from Sigma-Aldrich (Shanghai Branch, China). 1,2-Dipalmitoyl-*sn-glycero*-3-phosphocholine (DPPC) was purchased from Avanti Polar Lipids, Inc. (Alabama, USA).

1,2-Distearoyl-*sn-glycero*-3-phosphoethanolamine-*N*-[methoxy-(polyethyleneglycol)-2000] (DSPE-PEG2000) was purchased from Laysan Bio Inc (Alabama, USA). Unless otherwise mentioned, all other chemicals were purchased from Sigma-Aldrich. All solvents and chemicals were used as received.

2.2 Preparation of RE ($NaGdF_4$:Nd 5%@$NaGdF_4$) nanoprobes

2.2.1 Synthesis of $NaGdF_4$:Nd 5%.— $Gd(CH_3COO)_3{\cdot}xH_2O$ (972 mg, 1.9 mmol) and $Nd(CH_3COO)_3{\cdot}xH_2O$ (32 mg, 0.1 mmol) were added to a 100 mL three neck round-bottom flask containing octadecene (30 mL) and oleic acid (12 mL). The resulting solution was stirred magnetically and heated to 120 °C under vacuum (heating rate: 3 °C min^{-1}) to form lanthanide–oleate complexes. The solution was degassed at 120 °C for 15 min to remove residual water, acetic acid, and oxygen. The temperature of the solution was then lowered to 50 °C and the reaction flask was placed under a gentle flow of Ar. During this time, a solution of ammonium fluoride (296 mg, 8.0 mmol) and sodium hydroxide (200 mg, 5.0 mmol) dissolved in methanol (20 mL) was prepared *via* sonication. Once the temperature of the reaction mixture reached 50 °C, the methanol solution was added to the reaction flask and the resulting cloudy mixture was stirred for 30 min at 50 °C. The temperature of the reaction was then increased to ~70 °C, and the reaction mixture was degassed for 15 min to remove methanol. The reaction flask was then placed under a gentle flow of Ar. Subsequently, the reaction temperature was increased to 300 °C (heating rate: 20 °C min^{-1}) under Ar flow and this temperature was maintained for 90 min. The mixture was allowed to cool to room temperature naturally. The nanoparticles were precipitated by the addition of ethanol (~80 mL) and isolated *via* centrifugation at 5000 rpm. The resulting pellet was dispersed in a minimal amount of hexane (5–10 mL) and precipitated with excess ethanol (~60 mL). The nanoparticles were isolated *via* centrifugation at 5000 rpm and then dispersed in hexane (10–15 mL) for the subsequent shell growth step.

2.2.2 Synthesis of $NaGdF_4$:Nd 5%@$NaGdF_4$.— $Gd(CH_3COO)_3{\cdot}xH_2O$ (1023 mg, 2.0 mmol) was added to a 100 mL three neck round-bottom flask containing octadecene (30 mL) and oleic acid (12 mL). The solution was stirred magnetically and heated to 120 °C under vacuum (heating rate: 3 °C min^{-1}) to form lanthanide–oleate complexes. The solution was degassed at 120 °C for 15 min to remove residual water, acetic acid, and oxygen. The temperature of the solution was then lowered to 50 °C and the reaction flask was placed under a gentle flow of Ar. Then, a dispersion of $NaGdF_4$:Nd 5% core nanoparticles in hexane was added to the flask. During this time, a solution of ammonium fluoride (296 mg, 8.0 mmol) and sodium hydroxide (200 mg, 5.0 mmol) dissolved in methanol (20 mL) was prepared *via* sonication. Once the temperature of the reaction mixture reached 50 °C, the methanol solution was added to the reaction flask and the resulting cloudy mixture was stirred for 30 min at 50 °C. The temperature of the reaction was then increased to ~70 °C and the mixture was degassed for 15 min to remove methanol in the reaction flask. Then, the reaction flask was placed under a gentle flow of Ar. Subsequently, the temperature of the

reaction was increased to 300 °C (heating rate: 20 °C min^{-1}) under an Ar flow and maintained at this temperature for 90 min. The mixture was allowed to cool to room temperature naturally. The nanoparticles were precipitated by the addition of ethanol (~80 mL) and isolated *via* centrifugation at 5000 rpm. The resulting pellet was dispersed in a minimal amount of hexane (5–10 mL) and precipitated with excess ethanol (~60 mL). The nanoparticles were isolated *via* centrifugation at 5000 rpm and then dispersed in hexane (10–15 mL) for the subsequent shell growth step.

2.3 Fabrication of liposome-coated $NaGdF_4$:Nd 5%@$NaGdF_4$

Liposomes were made from a mixture of DPPC/Chol/DSPE-PEG2000 at a molar ratio of 77.5 : 20 : 2.5. The lipid (50 mg) was dissolved in 10 mL of ethanol in a round bottom flask. Ethanol was evaporated using a rotary evaporator at 55 °C. The lipid membrane was then hydrated with 5.0 mL of saline at 55 °C for 15 min. Finally, 10 mg mL^{-1} liposomes were obtained after sonication. $NaGdF_4$:Nd 5%@$NaGdF_4$ was dispersed in water at the same concentration of 10 mg ml^{-1}. $NaGdF_4$:Nd 5%@$NaGdF_4$ and liposome suspensions were both kept in a water bath at 55 °C for 5 min and mixed at a volume ratio of 1 : 2 ($NaGdF_4$:Nd 5%@$NaGdF_4$: liposome). After sonication at 55 °C for 5 min, the liposomes were fused with $NaGdF_4$:Nd 5%@$NaGdF_4$ to form $NaGdF_4$:Nd 5% @$NaGdF_4$@Lips (Gd-REs@Lips), which was collected by centrifugation at 12 000 rpm for 10 min.

2.4 Materials characterization

The absorbance spectra of the samples were recorded on an Agilent UV-Vis-NIR Cary 60 spectrometer (Agilent, Dongnan Tech Ltd). The NIR-II fluorescence emission spectrum was captured on a home-built spectroscopy set-up by excitation with an 808 nm laser diode with a power output of 100 mW. The excitation laser was filtered using a combination of 900 nm short-pass filters. The samples were added to a 1 cm path-length cuvette and the resulting emission filtered through a 1000 nm long-pass filter (Thorlabs, Aoyu Tech Ltd) to reject the incident excitation laser light. The emitted fluorescence was collected using a spectrometer coupled to a cooled (−80 °C) InGaAs detector array (NIRvana: 640; Princeton Instruments, Solartron, PAR-Ametek). The morphology of the nanoparticles was measured by transmission electron microscopy (TEM) using a JEOL JEM1400 transmission electron microscope (Ou Pu LTD).

2.5 *In vitro* cytotoxicity assay and *ex vivo* histologic analysis of organs from exposed mice

The cytotoxicity of Gd-REs@Lips was assessed using an anti-proliferation assay (MTT assay) in the fibroblast cell line NIH-3T3. The cells were firstly cultured in 96-well plates at a density of 5×10^3 cells per well in Dulbecco's Modified Eagle's Medium (DMEM, high glucose, GIBCO, Yanhong Ltd) containing 10% fetal bovine serum (FBS, Thermo, Yanhong Ltd) and incubated in an atmosphere of 5% CO_2 at 37 °C for 24 h. The cells were then incubated with Gd-REs@Lips at various concentrations (250, 200, 150, 100, and 50 g mL^{-1}) for another 24 h. Culture medium was then removed from each well, and replaced with 100 μL of culture medium containing MTT solution (0.5 mg mL^{-1}). The plate was incubated for 4 h at 37 °C before 100 μL of DMSO was added and the absorbance was measured at 550 nm. The absorbance of the untreated cells was used as a control reference value for

calculating relative cell viability. Animal studies were performed in compliance with an Institutional Animal Care and Use Committee (IACUC) approval at Stanford University. Athymic nude (nu/nu) mice were obtained from Charles River Laboratories, Inc. (Cambridge, MA), 4–6 weeks of age, and kept under sterile conditions. Three mice were sacrificed 15 days after the injection of Gd-REs@Lips at a dosage of 3 mmol kg^{-1}. Major organs (heart, lungs, liver, spleen, and kidneys) were harvested, sectioned, and stained with hematoxylin and eosin (H&E) for the histology analysis of different organs of mice exposed to Gd-REs@Lips.

2.6 MRI and NIR-II fluorescence imaging of phantoms

To measure the MRI relaxation properties of the nanoprobe, a series of Gd-REs@Lips aqueous solutions were prepared in PCR tubes at varying concentrations (Gd^{3+} concentration at 0, 0.75, 1.5, 3.125, 6.25 and 12.5 mM) for MR phantom studies. All experiments were performed in a 3.0T micro MR scanner (MRS 3000 series, MR Solutions Ltd, UK). The longitudinal relaxation time (T_1) was measured using an inversion recovery (IR) sequence (time of inversion, TI = 500, 700, 900, 1100, 1300, 1500, 1700, 1900 and 2100 ms), and the transverse relaxation time (T_2) was measured using a multi-slice turbo spin echo sequence with 10 different echo times (repetition time/echo time = 5000/15, 30, 45, 60, 75, 90, 105, 120, 135, and 150 ms). The signal intensities (SI) for each region of interest (ROI) on the T_1 or T_2 map were measured for each concentration using ImageJ software, and was then used for calculating longitudinal relaxivity or transverse relaxivity (r_1 or r_2), respectively. The r_1 or r_2 of Gd-REs@Lips was calculated from the slope of the plot T_1^{-1} or T_2^{-1} (ms^{-1}) against the metal concentration of Gd^{3+} (mM).

To measure the NIR-II fluorescence imaging of the nanoprobe, Gd-REs@Lips at different concentrations (0, 0.375, 0.75, 1.5, 3.125, 6.25, 12.5, 25 and 50 mM) were prepared in PCR tubes, and they were excited using an 808 nm diode laser through an optical fiber and a collimator, with a power density of 0.33 W cm^{-2} and an exposition time of 150 ms. All NIR-II images were collected on a two-dimensional InGaAs array NIR-II system (Princeton Instruments, Solartron, PAR-Ametek). ImageJ software was used for analyzing the images.

2.7 MRI and NIR-II fluorescence imaging in an orthotopic mouse liver cancer model

2.7.1 Establishment of orthotopic xenografts from hepatocellular carcinoma (HCC) patient specimens.—

This research was conducted ethically in accordance with the World Medical Association Declaration of Helsinki. HCC tissues were collected from HCC patients who had undergone liver resection as a part of their treatment. This study was approved by, and performed in accordance with the guidelines from, the Institutional Review Board at Stanford University for the use of human subjects in medical research (IRB protocol 26562). Informed consent was obtained from each patient prior to liver resection. Animal studies were approved by and carried out in compliance with Institutional Animal Care and Use Committee and Stanford University's Administrative Panel on Laboratory Animals Care (APLAC number 22201).

Orthotopic HCC patient-derived xenograft (PDX) models were generated following previously described methods.[14] Briefly, single-cell suspensions digested from HCC patient

tumor tissue were suspended in 100 μL of Dulbecco's phosphate buffered saline (DPBS) (Invitrogen Life Technologies, Carlsbad, CA) and mixed with 100 μL of Corning Matrigel Membrane Matrix (354234, Corning, Bedford, MA). The cell suspension was then injected subcutaneously near the left shoulder of 6–8-week-old male NOD. *Cg-Prkdc*^{scid} *Il2rg*^{tm1Wjl}/SzJ mice (NSG mice). The breeding pairs of NSG mice were obtained from Charles River Laboratories Inc., Cambridge, MA, and breeding was done in-house according to the approved institutional protocol. To generate the orthotopic model, the subcutaneous HCC xenografts with luciferase expression were harvested and cut into ~2 mm^3 pieces and implanted onto the left lobe of the liver of another group of 6–8-week-old male NSG mice. MR and NIR-II fluorescence imaging were performed 3–4 weeks after the implantation of PDX.

2.7.2 *In vivo* MRI.—Three mice bearing orthotopic PDX received MR examination prior to the intravenous tail vein injection of the Gd-REs@Lips nanoprobe at a dosage of 400 μmol per kg body weight. MRI was performed on a 3T micro-MRI system (MRS 3000 series, MR Solutions Ltd, UK) at 10 min and 30 min after nanoprobe administration. All mice were anesthetized by inhalation of 2% isoflurane with oxygen-enriched air in the MRI scanner, and the mice were kept in the scanner without changing the position or magnetic field during the entire scanning procedure. Multi-slice coronal T_1-weighted images were obtained from the abdomen of each mouse by using a fast spin-echo sequence with fat saturation (TR/TE = 730/11 ms, number of experiment (NEX) = 4, echo train length = 2; thickness of slice = 1 mm and 12 slices), and axial T_2-weighted images were acquired with a fast spin-echo sequence (repetition time (TR)/echo time (TE) = 5000/68 ms, number of experiment (NEX) = 4, echo train length = 4; thickness of slice = 1 mm and 12 slices).

ImageJ software was used to analyze the images. The signal-to-noise ratio (SNR) was calculated using the equation: $SNR_{liver\ or\ tumor} = SI_{liver\ or\ tumor}/SD_{noise}$, where SI is the signal intensity of the liver or PDX on MR images and SD is the standard deviation of image noise. To assess the efficacy of the enhancement, the contrast-to-noise ratio (CNR) was calculated, where $CNR = (SNR_{tumor} - SNR_{liver})/SNR_{tumor}$.[15] CNRs before injection, and at 5 min and 30 min after the injection of the nanoprobe were then compared.

2.7.3 *In vivo* NIR-II fluorescence imaging.—To demonstrate the value of Gd-REs@Lips in detecting liver tumors during surgery, an incision was made, with the mice under deep anesthesia, to expose the abdomens of the mice right after MR scanning. The liver was examined with NIR-II imaging under laser excitation provided by an 808 nm diode laser through an optical fiber and a collimator (power density of 0.33 W cm^{-2} and an exposition time of 1000 ms). The mice were then sacrificed and major organs (liver, spleen, kidneys, heart and lungs) were harvested for further NIR-II imaging and pathology analysis. Images were analyzed using ImageJ software, and the signal intensities (SI) of various organs were acquired. The ratio between the normal liver and liver tumor was calculated as $ratio_{liver\text{-}cancer} = SI_{liver}/SI_{cancer}$.

2.8 Statistical analysis

All data are presented as mean ± SD. Means were compared using Student's *t*-test or one-way ANOVA. A 95% confidence level was chosen to determine the significance between groups, with *P* values of <0.05 indicating statistically significant differences.

3. Results

3.1 Characterization of the Gd-REs@Lips nanoprobe

Firstly, Gd-REs were synthesized using the thermal decomposition method in the organic solvent oleic acid. Secondly, we measured the Gd concentration in Gd-REs using inductively coupled plasma mass spectrometry (ICP-MS). The mass concentration of Gd in Gd-REs is 57.2 ± 2.6%, which is close to the theoretical Gd concentration (60.5%) in $NaGdF_4$:Nd 5% @$NaGdF_4$. By manually measuring over 100 particles, Gd-REs showed a uniform and discrete spherical shape with an average diameter of 24.6 ± 1.2 nm (Fig. 1A). Since the original oleic acid-stabilized Gd-REs were hydrophobic, further surface modification was needed for improving the dispersion of REs in water. In this study, liposomes were used to coat the hydrophobic Gd-REs. As shown in the TEM image (Fig. 1B), Gd-REs@Lips had a homogeneous size of 29.2 ± 1.5 nm with a liposome coating thickness of 2.2 ± 0.5 nm. Multi-absorption peaks of Gd-REs@Lips were observed in the UV-Vis/NIR absorption spectrum (Fig. 1C). Gd-REs@Lips exhibited dual emission at 1057 nm and 1335 nm (Fig. 1D) with a large Stokes shift (249 nm and 527 nm, respectively). The quantum yield of Gd-REs@Lips was calculated to be 0.36% at 1057 nm and 0.17% at 1335 nm under 808 nm excitation (IR26 as a reference 0.05% in 1,2-dichloroethane). The quantum yield of the NIR-II emission at 1335 is lower than that at 1057 nm. We therefore chose to use 1057 nm for NIR-II imaging in our study. The physicochemical stability of Gd-REs@Lips was assessed in phosphate buffered saline (PBS) and fetal bovine serum (FBS). As shown in Fig. 1E, the zeta potential of Gd-REs@Lips in FBS (−35.2 ± 4.5 mV) was higher than that in PBS (−29.6 ± 3.1 mV), confirming their good physicochemical stability and that they will not aggregate in blood *in vivo*. In addition, the optical stability of Gd-REs@Lips in PBS and FBS was evaluated with an 808 nm laser (0.33 W cm^{-2}). The NIR-II fluorescence emission intensity of Gd-REs@Lips did not decrease, suggesting the high photostability of Gd-REs@Lips (Fig. 1F). The excellent physicochemical and optical performance of Gd-REs@Lips proved that they were suitable for NIR-II and MRI imaging *in vivo*.

3.2 Cytotoxicity study of the Gd-REs@Lips nanoprobe

To test the potential cytotoxicity of the nanoprobe, we conducted MTT assay with one day exposure in NIH3T3 cells, and pathological analyses of mice organs were performed 15 days after the injection of the nanoprobe at a high dosage (3 mmol per kg body weight). MTT assay indicated that there were no significant differences ($P > 0.05$) in the proliferation of the NIH-3T3 cells between the non-treated group and groups treated with different concentrations of Gd-REs@Lips after 24 h of incubation (Fig. 2A). Histological examination of different organs from exposed mice ($n = 3$) demonstrated no tissue damage, necrosis, or formation of lesions in the major organs of exposed mice compared to control mice receiving no nanoprobe (Fig. 2B). Both *in vitro* cell viability and *ex vivo* pathological

examination demonstrated good biocompatibility and safety of the nanoprobe at the dosage tested.

3.3 MR and NIR-II imaging of phantoms

The relaxivity properties of the Gd-REs@Lips nanocrystals were found to be 0.247 (r_1) and 2.166 (r_2) mM^{-1} s^{-1} (Fig. 3A), yielding an r_2 : r_1 ratio of 8.76. On regular T_1-weighted images, the signal intensity of Gd-REs@Lips nanocrystals reached a peak at the concentration of 6 mM, and it was about 1.5 times the signal of pure water. At the concentration of 12.5 mM, the signal intensity of the contrast decreased instead of increasing. On T_2-weighted images, the signal intensity of Gd-REs@Lips nanocrystals continued to increase from high to low concentrations (Fig. 3C). NIR-II imaging of Gd-REs@Lips phantoms showed that the signal intensities increased with increasing concentration (Fig. 3B). These combined results suggested the potential of Gd-REs@Lips for dual-modality MR and NIR-II fluorescence imaging.

3.4 *In vivo* MR and NIR-II fluorescence imaging in a mouse model of HCC

3.4.1 MRI.—Based on the good biocompatibility, attractive *in vitro* MRI, and optical imaging properties of Gd-REs@Lips, *in vivo* MRI and fluorescence imaging were performed in an orthotopic PDX model of HCC. The signal intensity (SI) of the non-tumor liver decreased markedly by 0.49 ± 0.09 ($P < 0.05$) at 5 min and by 0.56 ± 0.04 ($P < 0.05$) at 30 min after the i.v. injection of the nanoprobe. The SI of the PDX tumor decreased insignificantly after nanoprobe injection, by 0.07 ± 0.13 ($P > 0.05$) at 5 min and 0.08 ± 0.07 ($P > 0.05$) at 30 min. Therefore, a dramatic increase of the CNR between the orthotopic PDX and non-tumor liver tissue was observed on T_2WI (Fig. 4), indicating that Gd-REs@Lips nanocrystals exhibited a good T_2 contrast effect *in vivo*, with the potential for high diagnostic accuracy of liver lesions, while on T_1WI, no visible changes were observed from the SI of either the non-tumor liver or PDX tumor at different time points (data not shown), indicating that the nanoprobe did not show an evident T_1 contrast effect *in vivo*.

3.4.2 NIR-II fluorescence imaging.—To facilitate NIR-II fluorescence imaging, the abdominal walls of the PDX-bearing mice were incised before imaging, therefore resembling the exploration of HCC lesions during surgery. Images showed that Gd-REs@Lips distributed mainly in the non-tumor liver of the mice due to the reticuloendothelial system (RES) interaction, with little distribution in the PDX tumor, leading to a negative contrast and clear visualization of the tumor (Fig. 5A and B). In all three mice studied, the orthotopic PDX tumors were clearly visible with an obvious low SI, which distinguished them from the surrounding non-tumor liver tissues. The average liver-to-tumor contrast was 2.1 ± 0.83 (mean ± SD) (Fig. 5C). In addition to single-tumor detection, NIR-II fluorescence imaging also detected satellite lesions on the liver surface in some cases that would have been easily missed by the naked eye (Fig. 5D), with the smallest lesions detected about 2 mm in diameter. Histological findings confirmed that these satellite lesions observed by fluorescence imaging were tumor tissues (Fig. 5E).

4. Discussion

Multifunctional nanoplatforms which integrate multiple functions to provide comprehensive information both pre- and intra-operatively have attracted tremendous attention. In particular, the NIR-II light response-based nanoplatforms hold great potential in enhancing cancer detection and border demarcation, due to their many advantages compared to conventional imaging nanoplatforms in the visible region between 400 and 700 nm, or in the NIR-I window between 700 and 900 nm.[11,16] Here, Gd-REs@Lips prepared in-house presented NIR-II fluorescence emission with good imaging quality *in vitro*. In our *in vivo* orthotopic PDX model of HCC, we demonstrated that our nanoprobe allowed a clear visualization of the primary PDX tumor, and also tiny satellite tumors on the liver surface (with a diameter as small as 2 mm). Our encouraging results lay the foundation for the use of NIR-II fluorescence imaging for cancer detection as well as for surgery guidance. While other groups have studied either single optical imaging or multiple modality imaging to improve HCC detection during surgery,[8,10,17–20] these probes were mainly used for NIR-I fluorescence imaging, which may limit further improvements of spatial resolution and penetration depth compared with NIR-II fluorescence imaging. A most recent study reported the first-in-human liver-tumour surgery guided by multispectral fluorescence imaging in the visible and near-infrared-I/II windows (using the dye indocyanine green).[21] They found that intraoperative NIR-II imaging provided a higher tumour detection sensitivity and a higher tumour-to-normal liver tissue signal ratio compared with NIR-I imaging, which showed not only a more promising clinical use of NIR-II imaging in tumor detection and surgery guidance but also demand for more effective and safe NIR-II imaging probes. Here, the Gd-REs@Lips results demonstrate the dual NIR-II imaging and MRI imaging with high photostability and physicochemical stability. Besides, the dual probes contain rare earth elements with low toxicity showing the perfect biocompatibility with tissues. Therefore, Gd-Res@Lips have promising clinical translation in the future for NIR-II and MRI imaging applications.

In most research, the HCC tumors usually light up with the i.v. injection of molecular probes because of the EPR (enhanced permeability and retention) effect, biliary excretion disorders, or targeting to tumor biomarkers. In our study, though *ex vivo* fluorescence images of different organs showed that the signal intensity of the PDX model was higher than that of the heart, lungs and kidneys, indicating that there was an accumulation of our nanoprobe in the PDX model of HCC, it was still much lower compared with that of the liver and spleen. This phenomenon is probably associated with the global uptake of our nanoparticle by the RES[22–24] of the liver and spleen, showing the tumor as a “dark hole”, similar to the effect reported previously.[19]

MRI is now widely used for the diagnosis of major diseases such as tumors and cerebrovascular diseases, and there have been tremendous advancements in developing MRI contrast to further improve its sensitivity and detection capability. To date, gadolinium-based small molecular complexes are considered important contrast agents for T_1WI MRI, although it is known that gadolinium can shorten both T_1 and T_2.[25] Compared with the $GdF_3 : Nd^{3+}$ nanophosphor developed by Mimun *et al.*,[26] the r_1 value of Gd-REs@Lips is slightly higher (r_1 = 0.247 and 0.1481 on 3T and 7T, respectively). However, other Gd-based

nanoparticles with a smaller size show much higher r_1 values.[27–29] Johnson *et al.* studied the impact of size on the relaxivity of Gd-based contrast agents, and reported that their r_1 value increased dramatically with decreasing size from 3.0 mM^{-1} s^{-1} for 8.0 nm NPs to 7.2 mM^{-1} s^{-1} for the smallest 2.5 nm NPs.[26] The size of Gd-REs@Lips we prepared is about 30 nm, which may contribute to the low r_1 value of the nanoprobe. Therefore, further optimization is needed to prepare Gd-REs@Lips with a much smaller size but similar optical properties.

Generally, T_1WI is dominant with a low concentration of gadolinium-based contrast agents, while T_2WI is more dominant with a high concentration of gadolinium.[30] In MRI with standard clinically available contrast agents, the mild T_2-shortening effects of the standard doses of commercial gadolinium are usually overwhelmed by the more dominant T_1-shortening effects and therefore not normally observed. Interestingly, in our study, though the amount of gadolinium given to the mice is similar to the amount used in the clinic for T_1WI, the nanoprobes were taken up mostly by the non-tumor liver where they reached a high concentration quickly,[31] making the T_2WI effect more dominant. After injecting Gd-REs@Lips at a dosage of 400 μmol per kg body weight, we observed that the signal of the non-tumor liver on T_2WI decreased significantly by around 50–60%, which is comparable to that of the clinically used T_2WI contrast ferumoxides.[32] However, the signal of the tumor lesion did not decrease significantly, leading to a distinct contrast between the area of interest and its surroundings. The larger the difference in brightness between different tissue types, the easier it is to differentiate them from each other. The signal changes after the injection of Gd-REs@Lips led to the enhanced CNR between the liver and tumor, which makes the cancer lesions more prominent. Thus, this technique may help in identifying multiple and smaller HCC lesions with higher confidence.

5. Conclusions

In summary, we have successfully developed Gd-REs@Lips as a promising dual-modality nanoprobe that can serve as a negative contrast agent for both T_2-weighted imaging and NIR-II fluorescence imaging for HCC. The orthotopic PDX model used in our study provides high clinical relevance and gives us confidence that this nanoprobe has great applications in both research and clinical settings.

Acknowledgements

Prof. Y. Ren acknowledges the Visiting Scholar Program granted by China Scholarship Council (Grant No. 201808210152). The project was supported by the Natural Science Foundation of Liaoning Province, China (Grant No. 20180551174) and the Shenzhen Basic Research Project (No. JCYJ20170817094201000). This work was also partially supported by the fund from the Department of Radiology, Stanford University.

Notes and references

1. Forner A, Llovet JM and Bruix J, Lancet, 2012, 379, 1245. [PubMed: 22353262]
2. Bodzin AS, HepatoBil. Surg. Nutr, 2016, 5, 503.
3. El-Serag HB, Engl N. J. Med, 2011, 365, 1118.
4. Bray F, Ferlay J, Soerjomataram I, Siegel RL, Torre LA and Jemal A, Ca-Cancer J. Clin, 2018, 68, 394. [PubMed: 30207593]
5. Xu G, Qi F, Zhang J, Cheng G, Cai Y and Miao Y, World J. Surg. Oncol, 2012, 10, 163. [PubMed: 22897815]

6. Rahbari NN, Mehrabi A, Mollberg NM, Müller SA, Koch M, Büchler MW and Weitz J, Ann. Surg, 2011, 253, 453. [PubMed: 21263310]
7. Vahrmeijer AL, Hutteman M, van der Vorst JR, van de Velde CJH and Frangioni JV, Nat. Rev. Clin. Oncol, 2013, 10, 507. [PubMed: 23881033]
8. Lee J, Gordon AC, Kim H, Park W, Cho S, Lee B, Larson AC, Rozhkova EA and Kim D-H, Biomaterials, 2016, 109, 69. [PubMed: 27673597]
9. Yan H, Gao X, Zhang Y, Chang W, Li J, Li X, Du Q and Li C, ACS Appl. Mater. Interfaces, 2018, 10, 17047. [PubMed: 29708329]
10. Liu J, Li Z, Yang X, Liu W, Wang B, Zhu Y, Mu K and Zhu W, Chem. Commun, 2015, 51, 13369.
11. Kenry Y Duan and B. Liu, Adv. Mater, 2018, 30, 1802394.
12. He S, Chen S, Li D, Wu Y, Zhang X, Liu J, Song J, Liu L, Qu J and Cheng Z, Nano Lett, 2019, 19, 2985. [PubMed: 30983358]
13. He S, Song J, Qu J and Cheng Z, Chem. Soc. Rev, 2018, 47, 4258. [PubMed: 29725670]
14. Wei W, Wu S, Wang X, Sun CK-W, Yang X, Yan X, Chua M-S and So S, Oncotarget, 2014, 5, 5819. [PubMed: 25051375]
15. Zhao Z, Zhou Z, Bao J, Wang Z, Hu J, Chi X, Ni K, Wang R, Chen X, Chen Z and Gao J, Nat. Commun, 2013, 4, 2266. [PubMed: 23903002]
16. Bu L, Shen B and Cheng Z, Adv. Drug Delivery Rev, 2014, 76, 21.
17. Liu Y, Zhao Y-M, Akers W, Tang Z-Y, Fan J, Sun H-C, Ye Q-H, Wang L and Achilefu S, Transl. Res, 2013, 162, 324. [PubMed: 23747795]
18. Liu Y, Akers WJ, Bauer AQ, Mondal S, Gullicksrud K, Sudlow GP, Culver JP and Achilefu S, Analyst, 2013, 138, 2254. [PubMed: 23467534]
19. Ai T, Shang W, Yan H, Zeng C, Wang K, Gao Y, Guan T, Fang C and Tian J, Biomaterials, 2018, 167, 216. [PubMed: 29573651]
20. Huang S-W, Ou J-J and Wong HP, Transl. Gastroenterol. Hepatol, 2018, 3, 95. [PubMed: 30603731]
21. Hu Z, Fang C, Li B, Zhang Z, Cao C, Cai M, Su S, Sun X, Shi X, Li C, Zhou T, Zhang Y, Chi C, He P, Xia X, Chen Y, Gambhir SS, Cheng Z and Tian J, Nat. Biomed. Eng, 2020, 4, 259. [PubMed: 31873212]
22. Teston E, Richard S, Maldiney T, Lièvre N, Wang GY, Motte L, Richard C and Lalatonne Y, Chem. – Eur. J, 2015, 21, 7350. [PubMed: 25801438]
23. Maldiney T, Richard C, Seguin J, Wattier N, Bessodes M and Scherman D, ACS Nano, 2011, 5, 854. [PubMed: 21291197]
24. Anselmo AC, Gupta V, Zern BJ, Pan D, Zakrewsky M, Muzykantov V and Mitragotri S, ACS Nano, 2013, 7, 11129. [PubMed: 24182189]
25. Xiao Y-D, Paudel R, Liu J, Ma C, Zhang Z-S and Zhou S-K, Int. J. Mol. Med, 2016, 38, 1319. [PubMed: 27666161]
26. Mimun LC, Ajithkumar G, Pokhrel M, Yust BG, Elliott ZG, Pedraza F, Dhanale A, Tang L, Lin A-L, Dravid VP and Sardar DK, J. Mater. Chem. B, 2013, 1, 5702. [PubMed: 25584192]
27. Johnson NJJ, Chem. Mater, 2011, 23, 3714.
28. Zheng X-Y, Zhao K, Tang J, Wang X-Y, Li L-D, Chen N-X, Wang Y-J, Shi S, Zhang X, Malaisamy S, Sun L-D, Wang X, Chen C and Yan C-H, ACS Nano, 2017, 11, 3642. [PubMed: 28350963]
29. Johnson NJJ, He S, Nguyen Huu VA and Almutairi A, ACS Nano, 2016, 10, 8299. [PubMed: 27588579]
30. May DA and Pennington DJ, Radiology, 2000, 216, 232. [PubMed: 10887253]
31. Zhang Y-N, Poon W, Tavares AJ, McGilvray ID and Chan WCW, J. Controlled Release, 2016, 240, 332.
32. Chen F, Ward J and Robinson PJ, Magn. Reson. Imaging, 1999, 17, 549. [PubMed: 10231181]

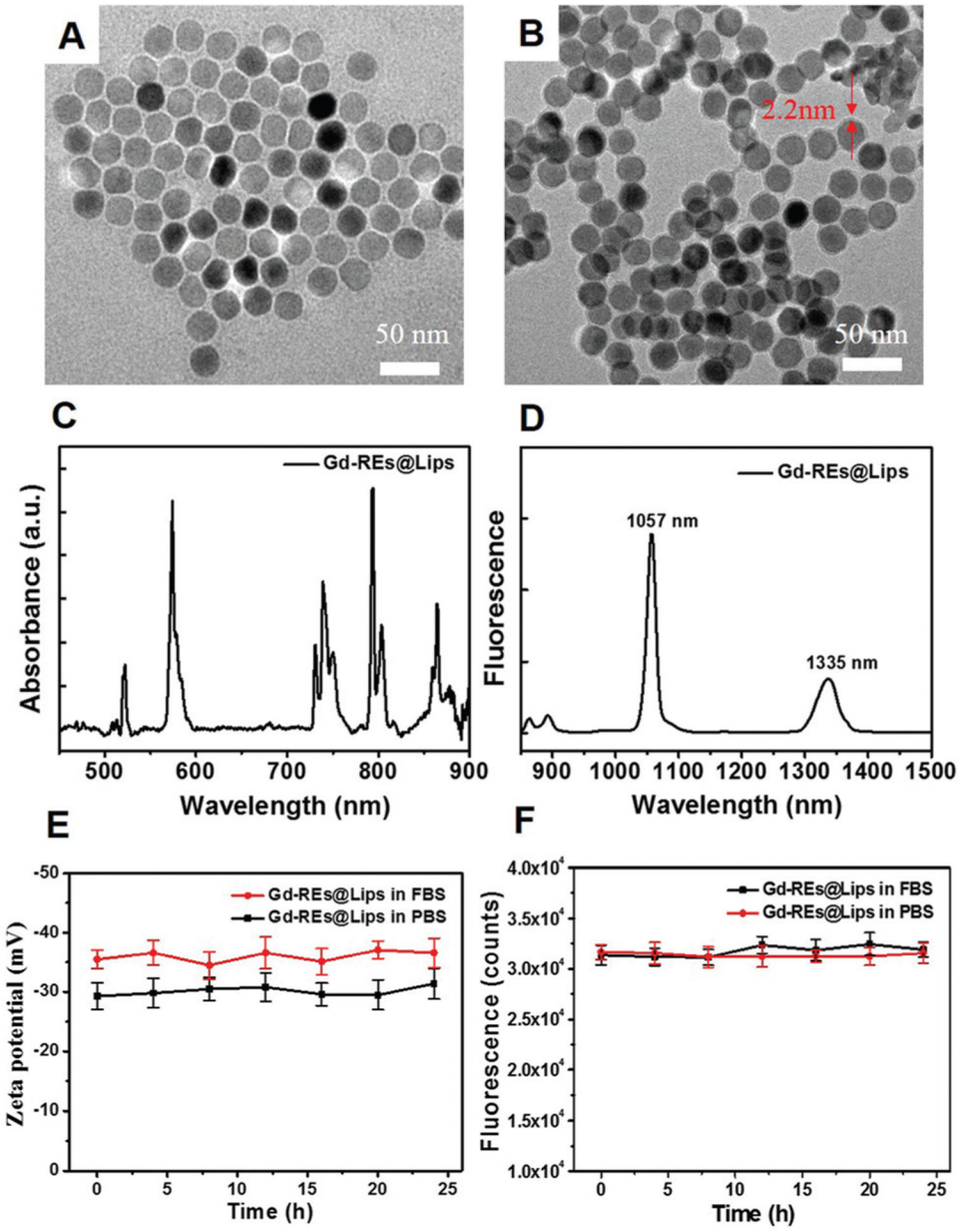

Fig. 1.

Characterization of Gd-REs@Lips. (A and B) TEM images of Gd-REs and Gd-REs@Lips. (C and D) Absorbance and fluorescence emission of Gd-REs@Lips. (E) Zeta potential of Gd-REs@Lips in FBS and PBS (as the control) for 25 h at 37 °C. (F) Photostability of Gd-REs@Lips in FBS and PBS.

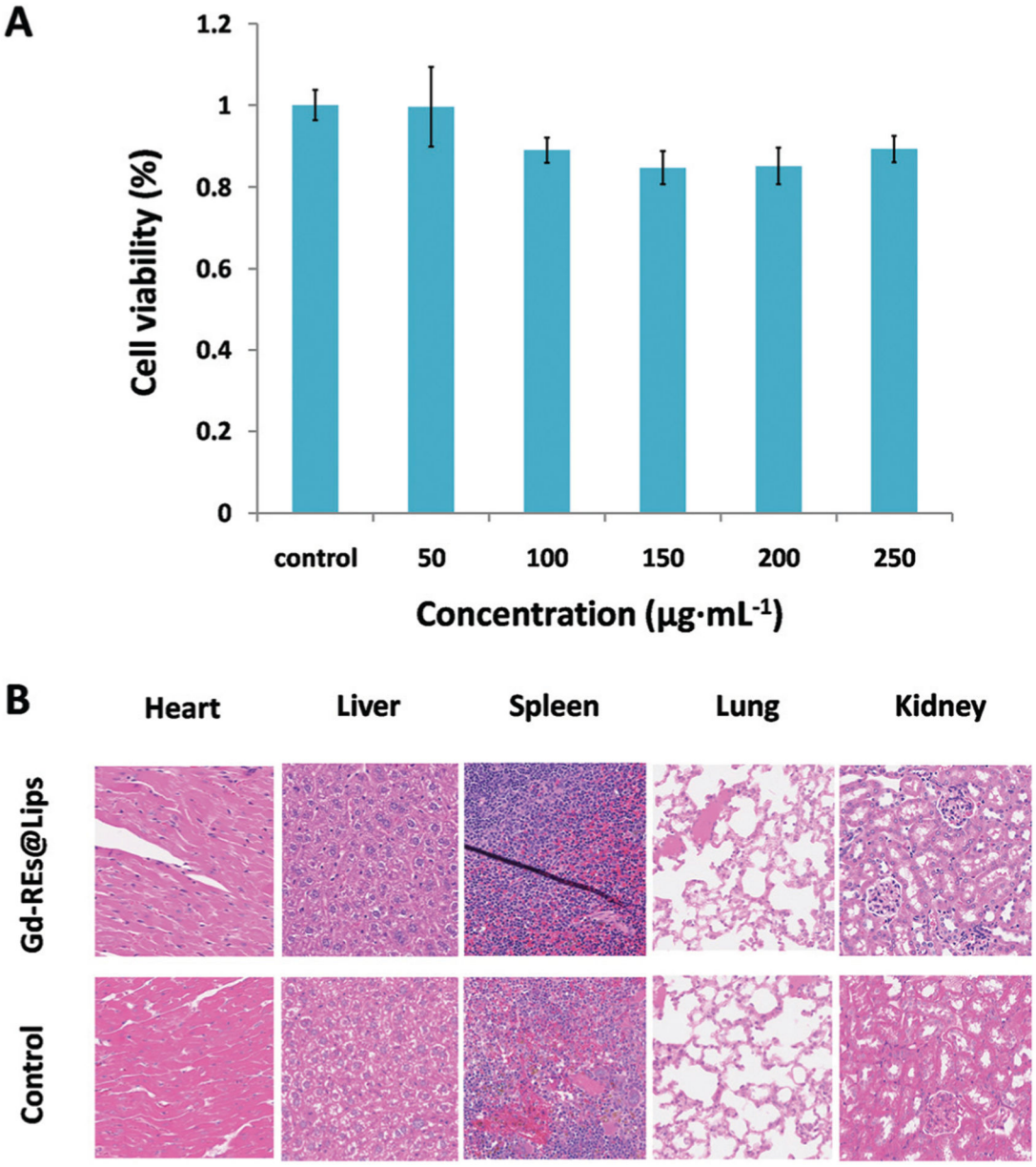

Fig. 2.

Biocompatibility study of Gd-REs@Lips. (A) Viability of NIH-3T3 cells after incubation with Gd-REs@Lips of different concentrations for 24 h at 37 °C. (B) H&E-stained tissue sections (×20) from mice without injection (control) and 15 days post-injection of Gd-REs@Lips at a dosage of 3 mmol kg^{-1}.

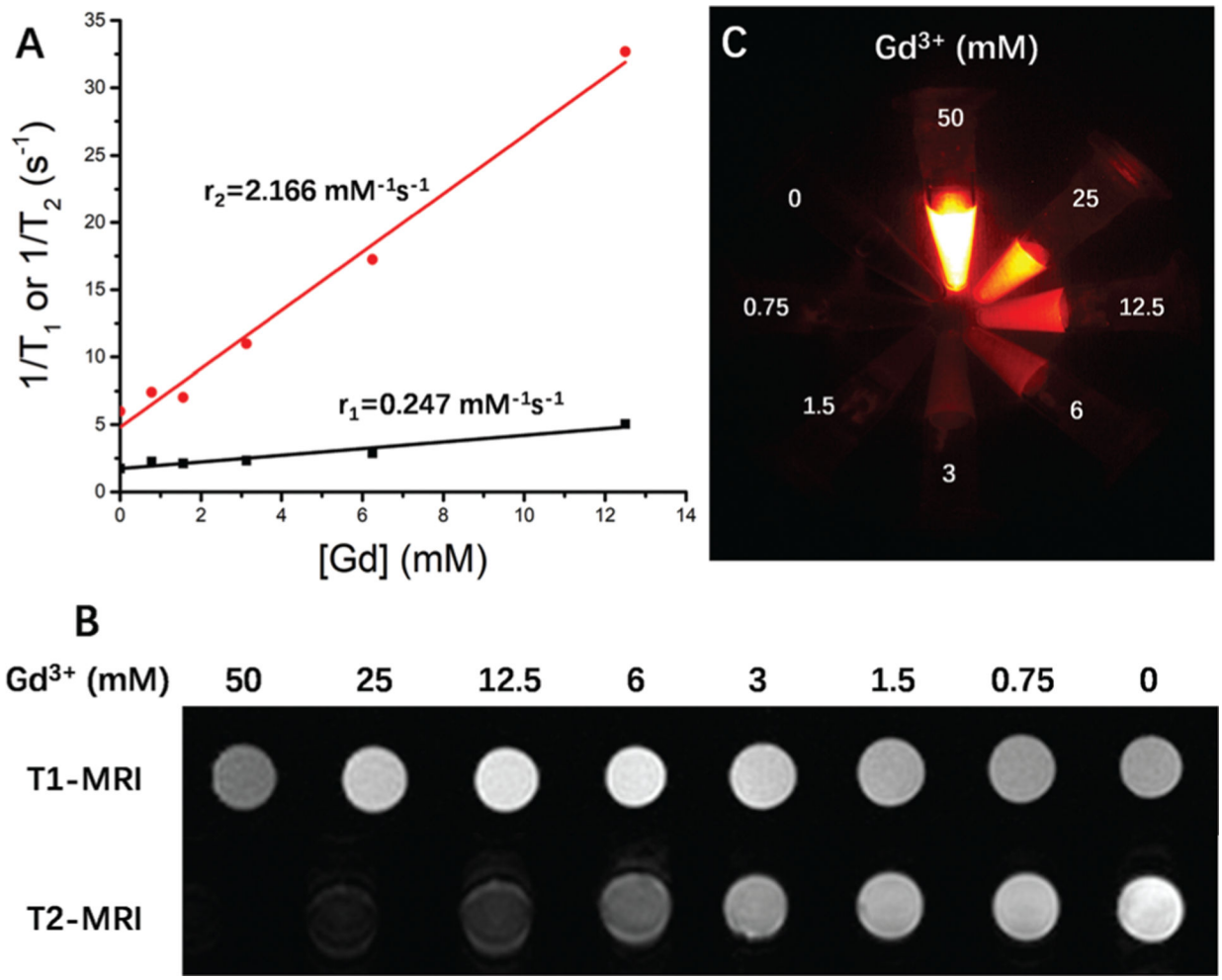

Fig. 3.

Phantom MR and optical imaging study of Gd-REs@Lips. (A) MR relaxivity (r_1 and r_2) of Gd-REs@Lips. (B) T_1-Weighted and T_2-weighted images of Gd-REs@Lips at different Gd concentrations on a 3.0T MRI scanner. (C) Phantom NIR-II imaging study of Gd-REs@Lips with different concentrations.

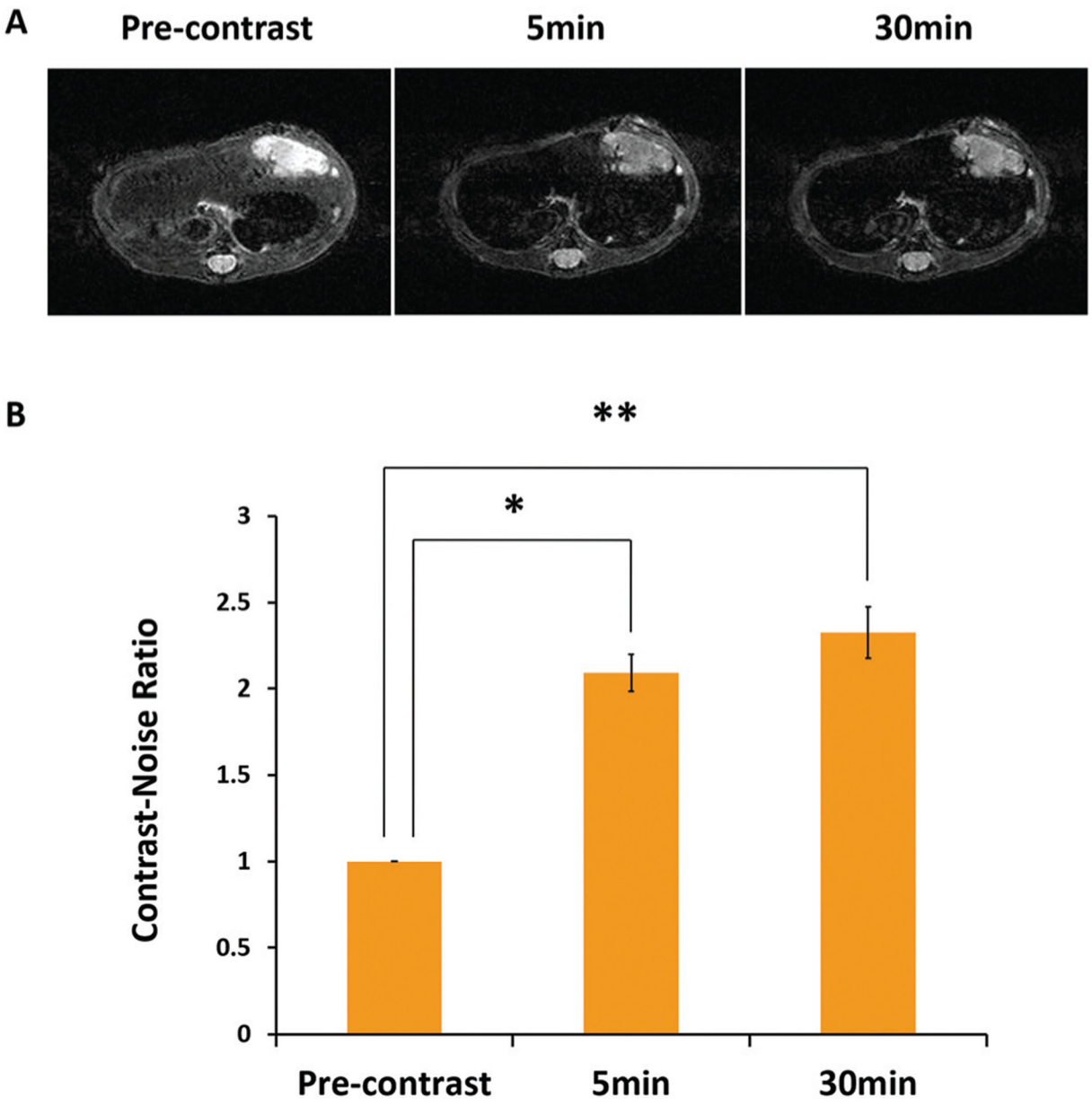

Fig. 4.

In vivo MRI study of Gd-REs@Lips on the orthotopic PDX mouse model of HCC. (A) T_2-Weighted images of mice before, 5 min and 30 min after tail vein injection of Gd-REs@Lips (n = 3). (B) Contrast-to-noise ratio (CNR) of non-tumor liver and PDX on T_2-weighted MR at different time points after the intravascular injection of Gd-REs@Lips.

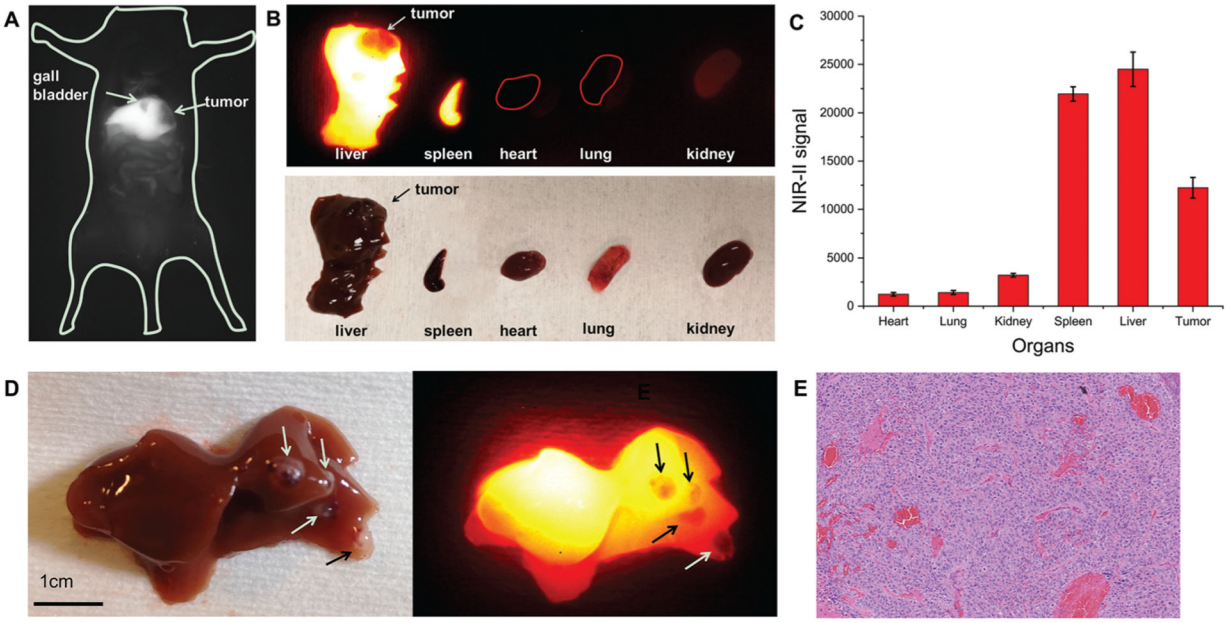

Fig. 5.

In vivo and *ex vivo* NIR-II imaging of mice bearing orthotopic PDX tumors ($n = 3$). (A) NIR-II window fluorescence imaging of liver tumor and gall bladder within the mouse abdomen. (B) *Ex vivo* fluorescence images of different organs. (C) *Ex vivo* quantification of NIR-II signal after organs were harvested. (D) Satellite liver lesions on the liver surface (arrows) (white light image on the left panel and NIR-II image on the right panel). (E) Histological examination of satellite liver lesion.